# Regimes of cloud vertical structure from active observations

**Dongmin Lee,[1,2] Lazaros Oreopoulos[2], Nayeong Cho,[2,3]**

[1] Morgan State University, Baltimore, Maryland

[2] Earth Sciences Division, NASA's Goddard Space Flight Center, Greenbelt, Maryland

[3] University of Maryland Baltimore County, Baltimore, Maryland

Corresponding author: Lazaros Oreopoulos (Lazaros.Oreopoulos@nasa.gov)

**Key Points:**

- Mixtures of cloud vertical structures from active observations and their large-scale model counterparts are amenable to classification.
- The classification enables the creation of a gridded dataset from data that were originally sparse in active observations.
- This dataset can be used to understand contributions to Earth energetics by various cloud systems in both observations and models.

## Abstract

We introduce a new type of cloud class, which we call "active cloud regime" (ACR), owing to its provenance from active (lidar and cloud radar) spaceborne cloud observations. ACRs intend to provide a climatological description based on cloud vertical structure (CVS) of the most prevalent monthly CVS mixtures encountered at large spatial scales of ~400 km. ACRs are thus a way to create a gridded dataset of a vertically-resolved cloud mask that can facilitate joint analysis with other gridded datasets. The detailed 2D cloud mask comes from the 2B-CLDCLASS-LIDAR CloudSat dataset fusing CALIPSO (lidar) and CloudSat (cloud radar) cloud detections. We show that the global classification of cloudiness under the ACR framework provides valuable insights on how the world's dominant cloud systems regulate the two major components of atmospheric energetics, precipitation and radiative cooling. NASA's GEOS model allows us to demonstrate the feasibility of applying the ACR concept in Earth System Models that have the capability to produce subgrid cloudiness obeying pre-specified vertical overlap rules. Comparison of observed and simulated ACRs provides thus another means to assess the realism of modeled clouds.



## Plain Language Summary

So-called "active" space-based observations such as those from backscatter lidars and cloud radars offer unique views of the vertical structure of clouds that enhance our understanding about many aspects of the planet's cloudiness and can be used to thoroughly assess clouds simulated by climate models. In this work we show that one way to compensate for the inherent sparseness of such observations is to group alike sparse products using standard classification schemes. The specific implementation of our study classifies previously derived instantaneous ~ 2 km cloud vertical structures into classes we call "active cloud regimes" defined at ~400 km domains and

resolved at monthly time scales. We show that this new cloud product enables easier probing of atmospheric energetics and evaluation of cloudiness simulated by large-scale models.

## 1. Introduction

Cloud views from active sensors such as the Cloud-Aerosol Lidar with Orthogonal Polarization (CALIOP) lidar (Winker et al. 2009) of the Cloud-Aerosol Lidar and Infrared Pathfinder Satellite Observation (CALIPSO) satellite and CloudSat's Cloud and Precipitation radar (CPR) (Stephens et al. 2002) provide information about certain aspects of clouds that is otherwise difficult to obtain from passive shortwave and thermal infrared imagers such as the Moderate Resolution Imaging Spectroradiometer (MODIS) and the Visible Infrared Imaging Radiometer Suite (VIIRS). Specifically, under a range of conditions, active sensors can more reliably detect cloud thermodynamic phase, the presence of multiple cloud layers, and cloud vertical structure, including the location of cloud top and base and the geometrical thickness of distinct cloud layers. In previous work we have taken advantage of this capability to generate distinct classes of cloud mask profiles we called Cloud Vertical Structures (CVS, Oreopoulos et al. 2017), as in Fig. 1. We also showed that Earth System Models equipped with a subcolumn cloud generator that incorporates vertical overlap rules can in principle also produce these major vertical cloud configurations inferred from individual observational "rays" of active sensors (Lee et al. 2020), and can thus have their cloudiness assessed with regard to the realism of their own cloud vertical configurations.

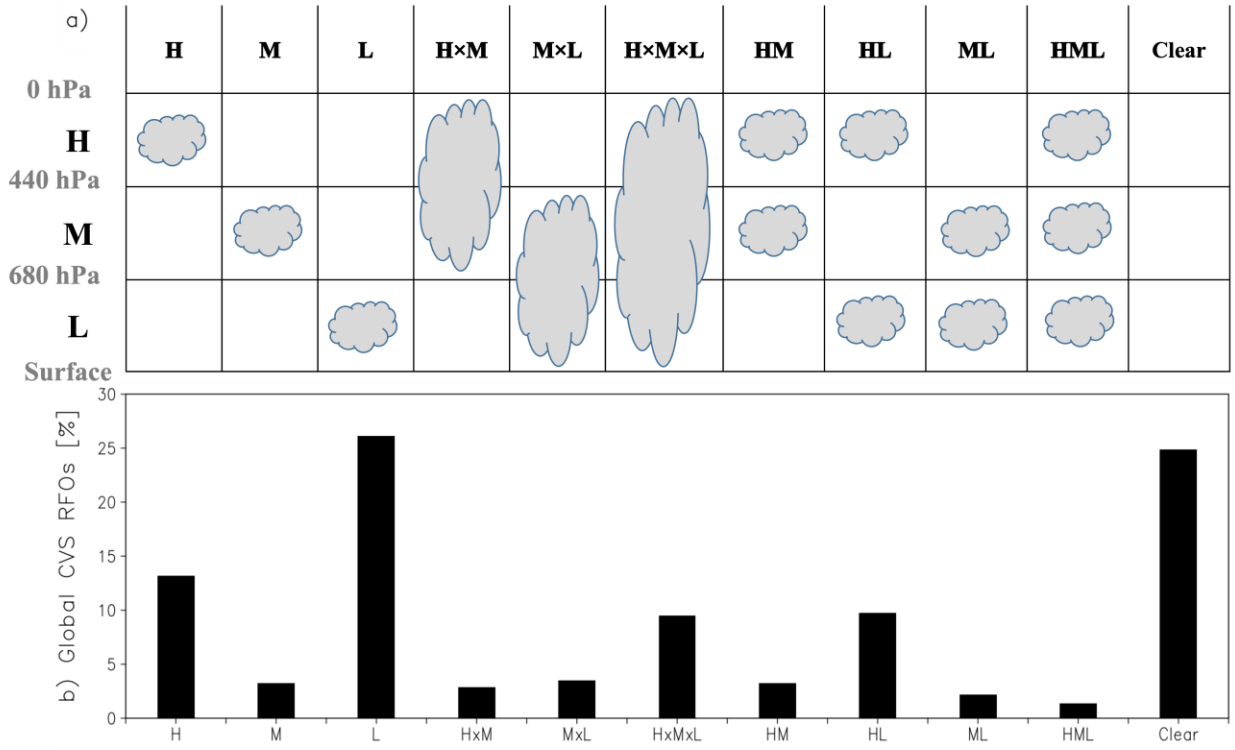


**Figure 1.** (a) The 10 CVS classes of Oreopoulos et al. (2017) representing co-occurrence combinations of high, middle, and low clouds (as defined by the International Satellite Cloud Climatology Project ISCCP) according to the CloudSat 2B-CLDCLASS-LIDAR (2BCL) product; (b) CVS global relative frequency of occurrence (RFO) from 2007-2010 observations, shown in histogram form.

Our previous work defined observed CVS at the fundamental spatial scale of the associated CloudSat-CALIPSO cloud product, 2B-CLDCLASS-LIDAR (henceforth "2BCL", Sassen et al. 2008), i.e., ~ 2 km. Conveniently, radiative fluxes at the boundaries of the atmospheric column, but also profiles of such fluxes throughout the column, associated with each CVS kind can be obtained from CloudSat's 2B-FLHXR-LIDAR (2BFL) product (Henderson et al. 2013). With appropriate averaging, this enables assessments of the overall long-term radiative impact of each CVS at either global or zonal scales (Lee et al. 2020). L'Ecuyer et al. (2019) performed a similar climatological radiative assessment, but based on

2BCL's "cloud type" classification. In these works, the gridded radiation composites obtained from radiative fluxes at ~ 2km horizontal resolution are specific to only the particular cloud class, be it CVS (Lee et al. 2020) or cloud type (L'Ecuyer et al. 2019); individual grid-averaged radiative fluxes cannot be associated with grid-averaged cloudiness since the latter is ill-defined. Effectively, one has to choose between either gridded radiative fluxes corresponding to unidentified mixtures of cloud classes, or construct a separate gridded radiation dataset for each cloud class. In either approach, the relationship between regional radiation and regional cloudiness cannot be resolved.

Given this state of affairs, this paper introduces the concept of a cloud class conveying vertical morphology that can serve as a gridded entity. We call this concept Active Cloud Regime (ACR). Such a gridded ("Level 3") cloud dataset, while by construction is much more coarsely resolved than its spatially sparse Level 2 progenitor, can be more straighforwardly combined with existing or tailored user-generated gridded products for studies aimed at gaining insight into the climatic role of distinct cloud vertical morphologies. An example of such an application in this work is the breakdown by ACR of the components of atmospheric diabatic heating which is accomplished by compositing independent monthly gridded datasets as a function of the mixtures of CVS kinds represented by ACRs.

In the remainder of the paper, we document the derivation of ACRs from observations and the cloud fields of a global model, and then show how they can be used to decompose and interpret various components of the Earth's energy budget. Performing such a decomposition on both observed and modeled ACRs, enables us to assess the realism of the model's cloudiness and distribution of energetics.

## 2. Dataset and derivation of Active Cloud Regimes

The fundamental concept applied to create a gridded cloud vertical structure dataset is classifying how various CVS (Fig. 1, see also Oreopoulos et al. 2017) mix over a chosen spatiotemporal scale. The relatively simple CVS classification of Fig. 1 introduced by Oreopoulos et al. (2017) adopted the International Satellite Cloud Climatology Project (ISCCP) convention of distinguishing clouds based on the altitude of their radiative top into high (*H*), middle (*M*), and low (*L*) categories using 680 and 440 hPa pressure levels as the delineating boundaries (Rossow and Schiffer 1999). The graphical depiction of Fig. 1 hopefully makes self-explanatory the nature of the different CVS kinds. In the CVS framework, the clouds encountered in each ~ 2 km profile of active observations are assigned to either one, two or all three of the ISCCP broad layers in which the troposphere is segmented; when they appear simultaneously in more than one, clouds can occupy adjacent layers either a contiguously (indicated by ×) or non-contiguously.

When CVS mix over a give spatiotemporal scale, the mixtures are expressed in terms of CVS frequency of occurrence (FOC) histograms. To construct these histograms we updated the CVS dataset previously used in Oreopoulos et al. (2017) with CVS from the newer 2BCL Release 5 (R05) dataset. As in that paper, we used four years of data from the 2007–2010 period belonging to the "golden" epoch of CloudSat–CALIPSO observations (i.e., before transition to daytime-only operations). We have chosen, for reasons explained below, 4° and one month as the underlying spatial and temporal scales on which CVS occurrences are accumulated into FOC histograms. While arbitrary, these scales were deemed suitable for the purposes of our classification as discussed below.

With the CVS mixtures expressed as histograms of CVS FOC at the aforementioned scales, their subsequent classification was accomplished by clustering via a *k*-means algorithm. The concept is fundamentally the same as the one used to classify into cloud regimes the passive imager

observations of cloud occurrences in specific cloud top pressure (CTP) and cloud optical thickness (COT) combinations ("cloud types") (e.g., Cho et al. 2021). In essence, instead of classifying a 42-element (combinations of 6 COT and 7 CTP bins) MODIS array of near-instantaneous cloud type occurrence in a 1° grid, here we classify an 11-element CVS FOC histogram (array) assembled from CVS occurrences over a month in a 4° domain. Examples of such histograms for two regions and two months are shown in Fig. 2. Note the large seasonal variability of CVS mixtures in both example regions, the Coral Sea and NE Pacific. The objective of the *k*-means clustering is to group FOC histograms like those in the four examples of Fig. 2 with alike histograms.

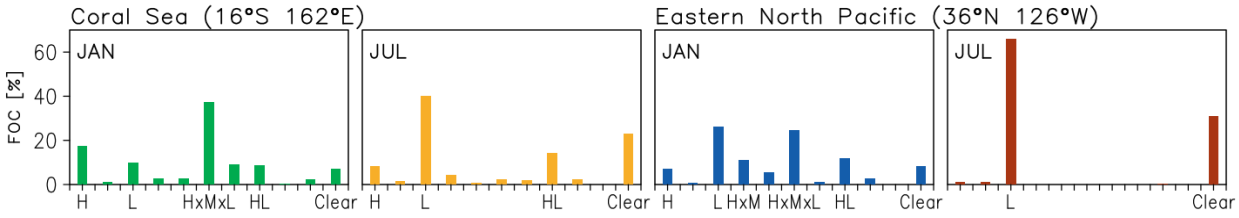


**Figure 2.** Four CVS FOC histogram examples from two select 4° regions and two different months (January and July). Large seasonal variations in CVS populations can be seen.

The 4° monthly spatiotemporal scale typically contains a large enough number of CVS samples (~$10^3$) to populate the histograms subjected to clustering. FOC histograms from even larger CVS populations could be produced by expanding the spatiotemporal scales, but this would bring drawbacks: first, cloud mixing would start becoming excessive to the detriment of the distinctiveness of the CVS mixture; second, the number of histograms furnished to the clustering algorithm would progressively become smaller, endangering algorithm convergence. With our current choice of spatiotemporal scales (four degrees monthly), geographical coverage (longitude from -180° to 180° and latitude from -82 to 82°) and length of dataset (48 months), 177120 (90×41×48) gridcells and corresponding histograms are available for the clustering process. The

bottom line is that with a fixed number of CVS samples, a judicial allocation needs to be made between CVS populations used to build FOC histograms and numbers of such histograms. Our trial and error with different spatial and temporal scales led to the conclusion that 4° and one month is indeed the Goldilocks choice of both robust, well-sampled, CVS FOC histograms, and also sufficient number of histograms for *k*-means clustering.

While objective methods of selecting the optimal number of clusters exist, they do not always yield physical results, so it is not uncommon common in *k*-means clustering to resort to some trial and error in order to settle on an appropriate number of clusters. In our case, after experimenting with different numbers of clusters $K$, we settled on $K$=10 as the best number of clusters to represent the ACRs. We found that fewer clusters muddled the geographical occurrence patterns and yielded less distinct peaks in the histogram centroids indicating too much mixing of dissimilar CVSs in the population. The additional separation provided by a larger number of clusters, on the other hand, was not as impactful as hoped for clusters that appeared to need splitting, and also made interpretation and analysis more unwieldy. One appealing aspect of our $K$=10 choice is the absence of extreme disparities in the resulting global RFOs of the ACRs (Fig. 3b): global ACR RFOs range between 5.7 and 15.1 indicating a rather balanced assignment of global cloudiness, with no ACR being overly rare or dominant.

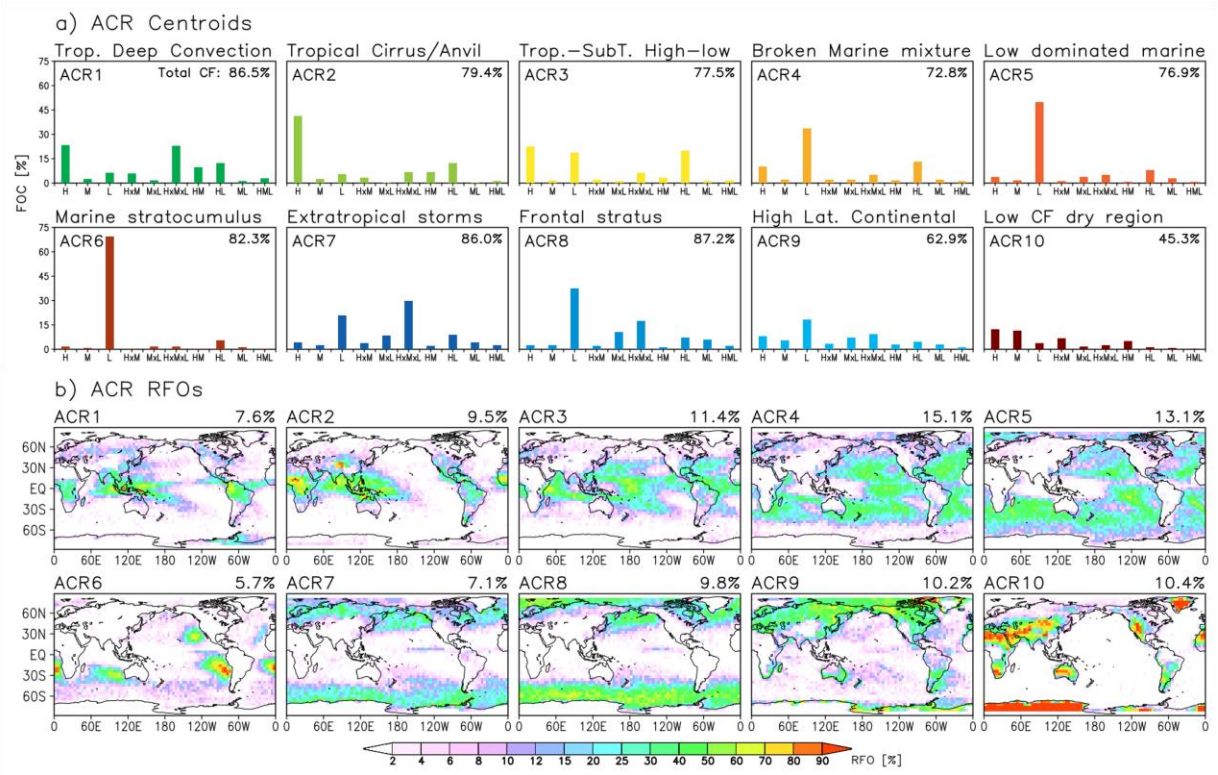


**Figure 3.** (a) Top two rows: observed ACR centroids, i.e., mean FOC histograms of the 10 CVS (non-clear) classes corresponding to the clusters obtained from the *k*-means algorithm for *K*=10 applied on monthly 4° data. Global cloud fraction values in % (100 minus FOC of clear CVS) are also shown in each panel. (b) Bottom two rows: geographical distribution of ACR RFO after assignment of 4° monthly FOC histograms to the closest ACR centroid. Global RFO values are shown at the top of each panel.

## 3. Observed ACRs

The two rows of Fig. 3a show the centroids of the derived ACRs, which are simply the mean histograms of all the monthly histograms of 4° grid cells that belong to the same cluster. The two rows of Figure 3b show the maps of relative RFO over the 4-year period; these were derived by assigning an ACR to each 4° gridcell based on minimum Euclidean distance between

its monthly histogram and the histogram representing the ACR centroid. The ACR centroids and their occurrence maps are key pieces of information for interpreting their makeup and nature.

- ACR1 comprises a mixture of CVS where isolated high clouds (CVS=*H*) and multi-layer vertically-developed cloud profiles that include high clouds (CVS=*H*×*M*, *H*×*M*×*L*, *HM*) occur at rates above climatology (compare with Fig. 1b). This ACR is more dominant in the tropics than anywhere else, so is interpreted as corresponding largely to tropical deep convection.

- ACR2 is also mostly of tropical nature and correlates geographically well with ACR1, but differs from it in that CVS=*H* dwarfs all other CVSs. ACR2 thus seems to contain much of the cirrus and anvil outflows of tropical convection. Some association with orography can also be seen (since the *H* designation is based on pressure level rather than height above ground).

- ACR3 is largely confined within the tropics and subtropics, but has more isolated low (CVS=*L*) clouds than the other two tropical ACRs, and in addition encompasses plentiful isolated high clouds, which along with the largest among all ACRs presence of CVS=*HL*, indicates also frequent co-existence of high and low clouds.

- ACR4 is a mixture of CVS that occupies most oceanic areas with the exception of the northernmost and southernmost latitudes, and the tropical western Pacific. While CVS=*L* is the most populous CVS kind, substantial amounts of high cloud are also present either in isolation or in co-occurrence with clouds at other levels. The average cloud fraction of ~73% indicates substantial occurrence of broken cloud conditions.

- ACR5 has similar geographical coverage as ACR4, but also extends further towards the poles. But it also encompasses a larger fraction of CVS=*L*, contains fewer high clouds, and its broken cloud conditions appear less prevalent.
- ACR6 seems to represent mostly marine stratocumulus clouds regimes. The dominance of CVS=*L* is unambiguous and average cloud fraction exceeds 80%.
- ACR7 is a high latitude marine cloud regime that approaches overcast conditions and is apparently associated with cyclonic and frontal systems. It has more vertically-developed clouds *H*×*M*×*L* than even ACR1, indicating that precipitating systems are frequently embedded in this ACR.
- ACR8 is similar to ACR7 in geographical coverage, but appears to correspond to weaker systems with more CVS=*L* clouds and fewer vertically developed systems *H*×*M*×*L*. Average cloud fraction nevertheless remains very high.
- ACR9 stands for a mixture of CVS that is mainly continental in nature, is mostly concentrated at high latitudes, is quite broken, and has no clear orographic association; it does not appear to be closely linked to weather systems.
- ACR10 is a low cloud fraction ACR occurring over mountainous and dry areas (deserts, Antarctica). A significant proportion of its CVS=*H* and CVS=*M* (largest proportion among all ACRs) likely comes from clouds over areas of high relief.

## 4. GEOS ACRs

The atmospheric GEOS model (https://gmao.gsfc.nasa.gov/GEOS_systems/, Rienecker et al., 2008) can also produce CVS as discussed in Lee et al. (2020) thanks to the implementation of the Räisänen et al. (2004) stochastic subcolumn generator. In order to produce counterpart GEOS

CVS, we run a prescribed sea surface temperature (SST) simulation at 1° resolution and over the same period as the observations with a version of GEOS ("v10.21.0") that has descended from the model version used in Lee et al. (2020). As explained in Lee et al. (2020), because the model cloud profiles can be a lot more complex than in observations, prohibiting a meaningful application of the Oreopoulos et al. (2017) CVS classification algorithm, the model's CVS kinds were reduced from 10 to 7 by combining the multilayer categories comprising clouds in the adjacent standard vertical layers (delineated by the 680 hPa and 440 hPa pressure levels). With the distinction between contiguous and non-contiguous clouds across the standard layers eliminated, the observed ACR centroids are then also expressed in terms of the reduced set of 7 CVS as seen in Fig. 4a. This figure, in contrast to Fig. 3, uses a stacked bar representation of each ACR's CVS composition. The model's 7-element CVS FOC histograms over a month in 4° regions were assigned to the closest (according to minimum Euclidean Distance – the squared difference of FOC between observed an observed histogram and a centroid) of the 10 observed (and simplified) ACR centroids. The means of the histograms assigned to each ACR resulting from this procedure represent the GEOS ACR centroids; these are also shown in Fig. 4a as stacked bars to the right of their observational counterparts.

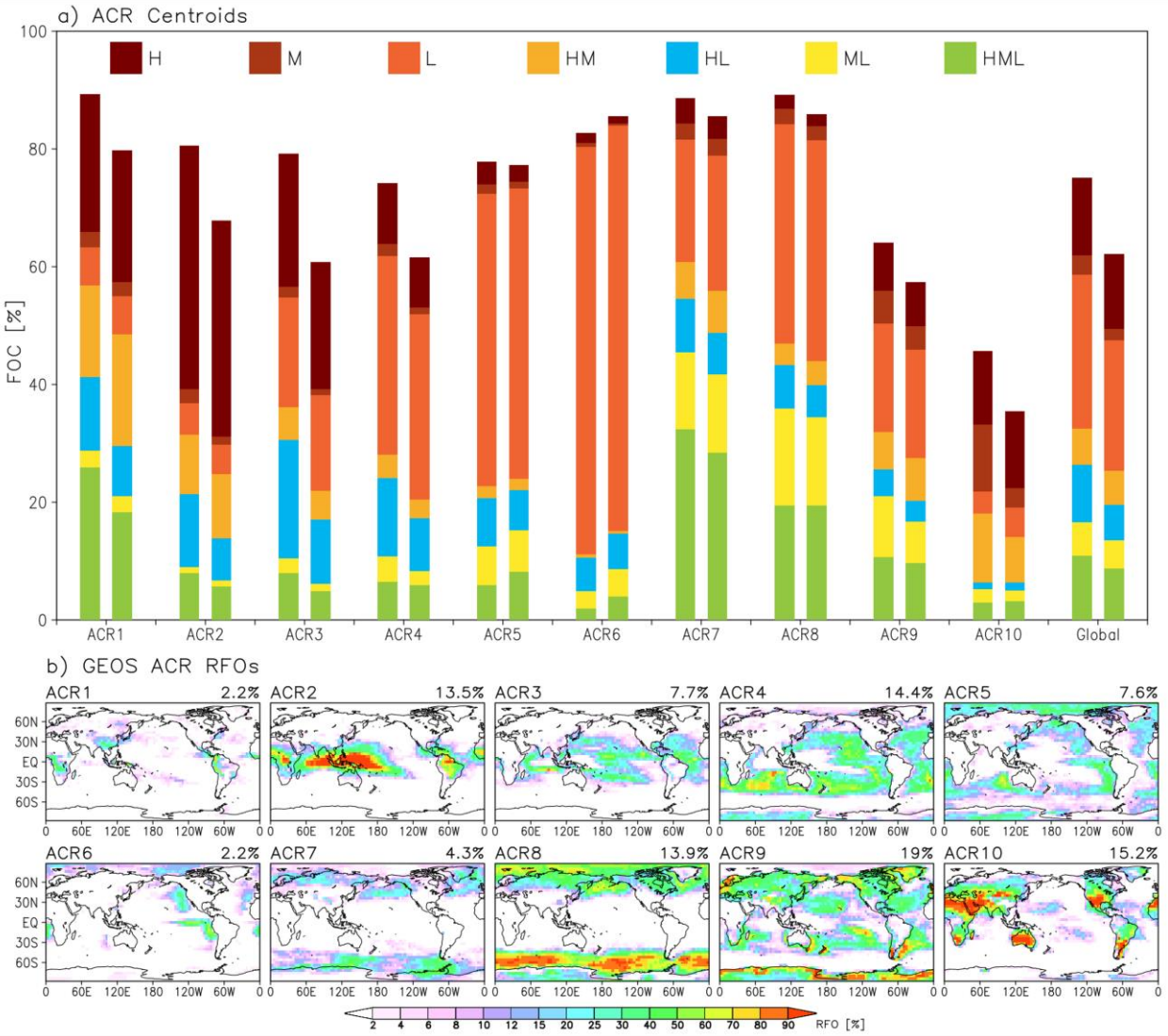


**Figure 4.** (a) ACR centroids from observations (first bar of pair) and GEOS (second bar of pair) from monthly FOC histograms in 4° regions resolved into the reduced set of 7 CVS classes (see text for explanation). A different visualization than Fig. 3 is used here where each centroid is represented by a stacked bar containing the CVS FOC. (b) RFO maps of GEOS ACRs after CVS FOC assignment according to minimum Euclidean Distance. Global RFO values are shown at the top of each panel.

One can see that the observed and modeled ACR centroids exhibit considerable similarity. This is largely by design because of the "forced" assignment of modeled CVS FOC histograms to the

235 closest, in terms of Euclidean distance, observed ACR centroid. Even when the resemblance of
236 modeled histograms assigned to an observed ACR is imperfect, it is still better than that for other
237 ACRs, making the modeled ACR centroid (mean of modeled histograms) a reasonably close
238 (albeit flawed) kin of its observed counterpart. While individual occurrences of simulated ACRs
239 represent clouds similar to those in observed members of the same real-world ACR, the overall
240 frequency and locations at which alike simulated CVS histograms tend to occur differs from
241 observations, ultimately resulting in substantial discrepancies in geographical characteristics and
242 global occurrence statistics. This can be readily noticed when comparing the RFO maps of
243 GEOS ACRs in Fig. 4b with the counterpart maps of observed ACRs shown in Fig. 3b. Focusing
244 on differences in global and geographical RFO between observations and model of similar ACRs
245 allows for a much more straightforward interpretation of cloudiness differences than performing
246 clustering on modeled CVS FOC histograms; such an approach would have likely led to very
247 different ACRs, and would have made comparisons quite cumbersome.

248 When comparing global cloud fractions (sum of FOCs of all CVS other than the clear CVS), the
249 observed and modeled ACRs that differ the most, in spite of our "forced" assignment, are ACR1,
250 ACR2, ACR3, ACR4, and ACR10. The global cloud fraction differences arise in turn from
251 differences in the global FOC of certain constituent CVS kinds.The GEOS version of ACR1 is
252 overall less extensive, event though it has proportionally far more isolated CVS = *H* clouds. This
253 is because it also has far fewer vertically deep CVS = *HML* clouds (recall that this category now
254 includes CVS = *H*×*M*×*L* which are far more numerous in observations than original *HML*), and
255 also fewer CVS = *HL* clouds. Observed isolated CVS = *H* clouds are frequently encountered in
256 CVS mixtures that belong to ACR2, but *H* clouds in the GEOS version of ACR2 are less
257 common. Underestimates of CVS = *HL* are notable in modeled CVS FOC histograms assigned to
258 ACR4, but this issue seems to be related to the broader deficiency of too few low clouds in

GEOS (see ACR4's discrepancy for CVS=*L*). Even when the two ACR versions have similar cloud fractions, this is the result of compensations of inconsistent contributions from different CVSs. ACR5 is an example of such a situation: the model has more CVS = *HML* clouds, but this is compensated by fewer CVS = *H* and *HL* clouds.

When ACR global RFOs and (normalized) regional frequencies are examined, even more discrepancies between model and observations emerge (contrast the maps of Figs. 3 and 4 and the accompanying global RFO values of each panel). The global RFO is substantially different for all ACRs except ACR4, for which the modeled geographical distribution is actually also quite realistic. The model's convection seems to be expressed mostly via a generous production of CVS = *H* clouds which are featured in ACR2, to the detriment of CVS = *HML* clouds featured in ACR1, making ACR1 quite rare in GEOS. ACR3 is quite reasonably simulated in the model; but this not the case for ACR6, with apparently many of the model's marine stratocumulus (CVS = *L* clouds) going to to ACR5. But ACR5 on the other hand suffers from little southern ocean presence, as it is replaced in that region by ACR8. While ACR9 is mostly continental in observations, it has nearly as much oceanic presence in GEOS and emerges as the most populous ACR. Finally, the model seems to have a cloudier Antarctic continent, with ACR4, ACR5, ACR8, and ACR9 presence, whilst in the observations the least cloudy ACR10 dominates.

In the following section we examine how these differences translate to biases in the breakdown by ACR of radiative flux and diabatic heating. The analysis reveals that even if overall the model's global cloudiness values are (unsurprisingly) close to observations, their distribution among the world's major cloud systems, expressed via ACRs, remains deficient.

## 5. Energetics of observed vs modeled ACRs

This section examines how the world's cloud systems, when classified via ACRs, regulate major energetic components of the atmosphere and the planet as a whole. First, we look at how ACRs change radiative fluxes and heating rates with respect to cloudless skies in both the shortwave (SW) and longwave (LW) part of the spectrum, and then how they affect the atmospheric diabatic heating, especially the dominant radiative and latent heat components.

### *5.1 Integrated cloud radiative effects in the atmosphere-surface column*

The Cloud Radiative Effect CRE is the difference between net (down minus up) all-sky and clear-sky fluxes and serves as a measure of the impact of clouds on atmospheric radiative fluxes. The observed mean CRE of each ACR for SW (blue bars), LW (red bars), and total = SW+LW (purple bars) at the boundaries of atmospheric column, namely the top-of-the-atmosphere (TOA) and the surface (SFC) is shown in Fig. 5's top and bottom panels, respectively. The difference between TOA and SFC CREs is the atmospheric CRE which is shown in the middle panel. CRE comes from CERES-EBAF (Loeb et al. 2018; Kato et al. 2018), specifically the latest version Ed4.2 which provides monthly values on a 1° grid, and has thus been coarsened to 4° for our purposes to match the ACR spatial resolution. CRE is then averaged separately for each ACR. The ability to use CERES-EBAF in conjunction with CALIPSO and CloudSat cloud retrievals is a testament to the utility of the ACR concept. Vertical cloud masks from active observations originally resolved in the 2BCL dataset at ~2 km have been transformed into a gridded dataset via ACRs and can now be combined with another gridded dataset. The only previous choice for

combining radiative fluxes with CloudSat/CALIPSO 2BCL clouds was the 2BFL product (Matus et al. 2017; Oreopoulos et al 2017; L'Ecuyer et al. 2019; Lee et al. 2020).

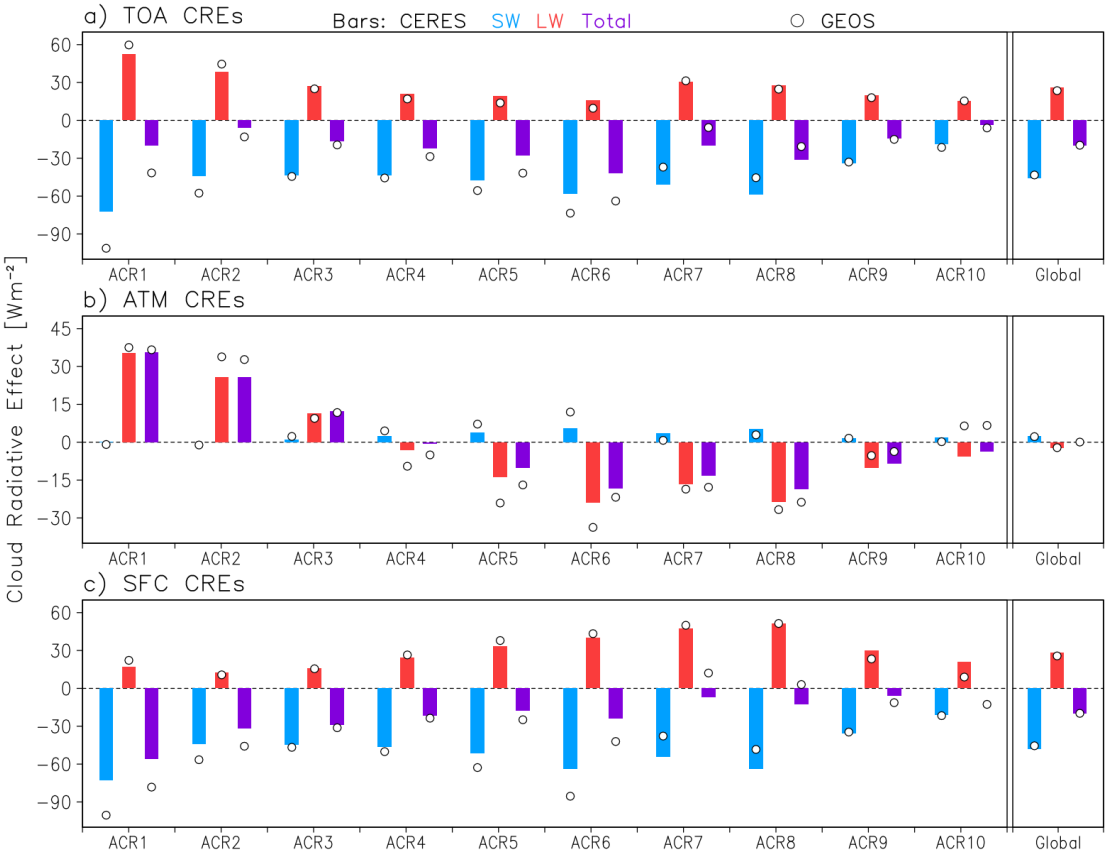


**Figure 5.** SW, LW, and total=SW+LW CRE from CERES-EBAF for (a) TOA , (b) ATM, (c) SFC averaged across ACR occurrences (i.e, not RFO-weighted which are shown in the Supplemental Material Fig. S1). Observed values are shown as bars while modeled values as open circles. TOA and SFC CRE is defined as the double difference between downward and upward all-sky minus clear sky fluxes. ATM CRE is the difference between TOA and SFC CRE.

Open circle symbols in Fig. 5 correspond to the counterpart CRE breakdown by ACR from GEOS. It is important to underscore that the CRE means are averages across ACR occurrences only, i.e., showcase the average strength of CRE for each ACR *when it occurs*. CREs weighted

311 by ACR RFO to indicate the contribution of each ACR to the global CRE are shown in the
312 Supplementary Information (Fig. S1). The TOA and SFC CREs indicate whether ACRs cool
313 (negative values) or warm (positive values) the planet as a whole (TOA) or its surface (SFC).
314 Their difference (ATM CRE) indicates how much ACRs reduce (positive values) or enhance
315 (negative values) the atmospheric clear-sky radiative cooling. The SW ATM CRE is typically a
316 small positive value or near zero (due to the competition between added cloud absorption and
317 reduced water vapor absorption below clouds), while the LW ATM CRE can be either positive
318 or negative.

319 Figure 5 illuminates various interesting aspects of the global radiative role of ACRs. All ACRs
320 have a planetary cooling effect, as seen by the negative purple bars at the TOA, stemming from
321 the SW CRE being larger in absolute value than the LW CRE. They also have a cooling effect at
322 the surface across all ACRs, but the magnitudes of total CRE differ at the two boundaries. The
323 strongest TOA cooling corresponds to ACR6 dominated by CVS = *L* which has a much weaker
324 TOA LW CRE, because low clouds do not change much the height of atmosphere's effective
325 emission to space, than TOA SW CRE. But at the SFC where the SW CRE remains strong, the
326 LW CRE is also strong because the increased atmospheric opacity of low clouds at warm
327 tropospheric temperatures results in an enhancement in the downward LW flux. The weak
328 cooling at the SFC compared to the strong cooling at the TOA means that substantial cooling
329 occurs within the atmosphere. This is indeed shown by ACR6's purple bar in the middle panel of
330 Fig. 5. A similar behavior is also observed for ACR8 which has proportionally less CVS = *L*, but
331 apparently enough to behave similarly. Contrast this with ACR2 which has many CVS = *H*
332 clouds: SW and LW CRE at TOA almost cancel (near zero total CRE), but the SW CRE
333 dominates at the SFC (approximately the same value as in TOA, similarly to all other ACRs)
334 because the LW CRE is small: despite the added opacity, clouds are too high to have much of an

335 impact to the downwelling LW at the SFC which originates mostly from lower atmospheric
336 levels (in other words, ACR2 does not reduce much the effective height of downward emission).
337 This makes ACR2's surface cooling much stronger than its TOA cooling which in turns means
338 that large atmospheric warming takes place, something confirmed by the middle panel.

339 Figure 6 shows the annual zonal distribution of the contribution of each ACR to the TOA and
340 SFC SW and LW CRE. These plots are based on RFO-weighted CREs (the ACR zonal RFOs
341 themselves are shown in Fig. 9), and are similar to those in L'Ecuyer et al. (2019) who showed
342 zonal contributions to 2BFL CRE by 2BCL cloud types. In this type of plot the zonal CRE of
343 each ACR is added to the cumulative CRE of all ACRs that preceded it in our (somewhat
344 arbitrary) ordering of ACRs. So, for example, the zonal CRE values shown for ACR6 are
345 actually the cumulative CRE values from ACR1 to ACR6, and the ACR10 zonal values are thus
346 the cumulative zonal CRE contributions of all ACRs. For illustration purposes the area under the
347 curves representing the successive cumulative values is color-filled so that the incremental
348 contribution of each ACR to the zonal CRE values can be visualized by the area each ACR adds
349 to the cumulative zonal curve of all previous ACRs. The left column of panels shows observed
350 values from CERES EBAF, while the right column shows counterpart GEOS values. These
351 zonal plots make clear the tropical dominance in observations of ACR1 and ACR2 for SW and
352 LW TOA CRE, and SW SFC CRE; their LW SFC CRE contribution is more muted which is
353 consistent with the weak values of this CRE in the tropics where the high humidity of the lower
354 troposphere suppresses the downward longwave cloud emission reaching the surface. Fig. 6 also
355 reveals a strong hemispheric asymmetry at midlatitudes with ACR8 making much larger

356 contributions to all four CRE components in the Southern Hemisphere because of its large
357 presence in that part of the world (see ACR RFO panel in Fig. 9).

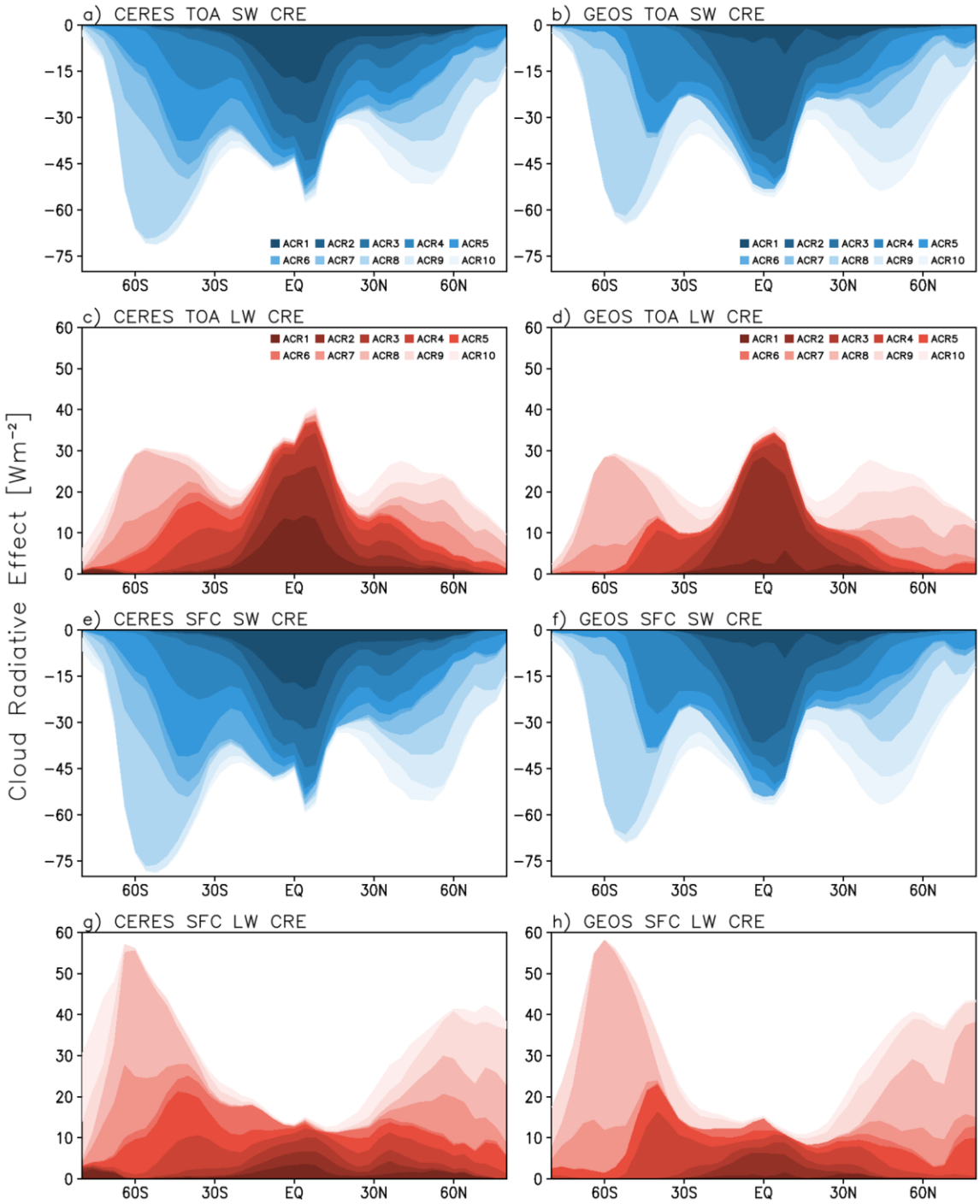


358

**Figure 6.** Contributions of each ACR to the annual zonal TOA and SFC SW and LW CRE from CERES EBAF RFO-weighted CRE values (the zonal values of the RFOs themselves are shown in Fig. 9). The values corresponding to each ACR are cumulative and include the contribution of that ACR along with that of all those that precede it in our ACR ordering. See text for more details. The left column of panels corresponds to observations while the right column to GEOS.

Figures 5 and 6 make apparent the great diversity of CRE stemming from the planet's various cloud systems. Given strong seasonal variations of solar illumination outside the tropics, even more SW CRE variability throughout the year would have been seen for ACRs prevailing at those latitudes, if seasonal CREs were to be examined. A lot of CRE diversity is also seen in GEOS (open circles in Fig. 5), but the breakdown of CRE by ACR generally deviates from observations with a few exceptions, such as ACR3 and ACR4. Also, when different CRE components are combined, e.g., adding SW and LW CRE or subtracting SFC from TOA CRE, the model can fortuitously approach the observed CRE. See for example how well ACR1's total ATM CRE is simulated despite large TOA and SFC discrepancies. Moreover, also note how well the model simulates the global CRE (rightmost part of the Fig. 5 panels): despite errors in the global CRE breakdown by ACR, when everything is added together the biases cancel out almost perfectly. The TOA and SFC CRE observation-model discrepancies at the ACR level can be further scrutinized with the Fig. 6 zonal plots. When comparing the panels of the left and right columns of Fig. 6 one can see again the contrast in ACR1 and ACR2 CRE contributions; the model's weaker SW CRE and weaker LW CRE in the in the Southern Hemisphere midlatitudes

379 and subtropics, respectively; and the bigger importance of its ACR8-ACR10 in the Northern
380 Hemisphere midlatitudes.

381 *5.2 Vertically resolved atmospheric cloud radiative effects*

382 The ATM CRE can be further resolved vertically using 2BFL flux profiles which we composite
383 by ACR for the 2007-2010 period. Since the 2BFL dataset matches spatiotemporally 2BCL, a
384 breakdown of vertically resolved ATM CRE over the same period could have also been
385 performed by CVS, and would have also been insightful, but would not reflect the reality of CVS
386 mixing regionally. Annual zonal averages (resolved in 4° latitude) of the vertically resolved
387 cloud radiative heating rate CRHR for each ACR for both observations and GEOS are shown in
388 Fig. 7a for LW, and Fig. 7b for SW. The CRHR is basically the difference of the net (down-up)
389 flux profiles between cloudy skies and clear skies expressed in units of K/day, and represents
390 physically the cloud-induced change of the radiative heating/cooling rate of clear skies. The
391 CRHRs of the ACRs add to the total CRHR shown in the leftmost panels of Fig. 7. The SI shows
392 counterpart seasonal (winter and summer) plots (Fig. S2) which allow us to glean radiative

393 effects on the atmosphere of seasonal movements of cloud systems in the two hemispheres and
394 to compare with similar plots by Haynes et al (2013).

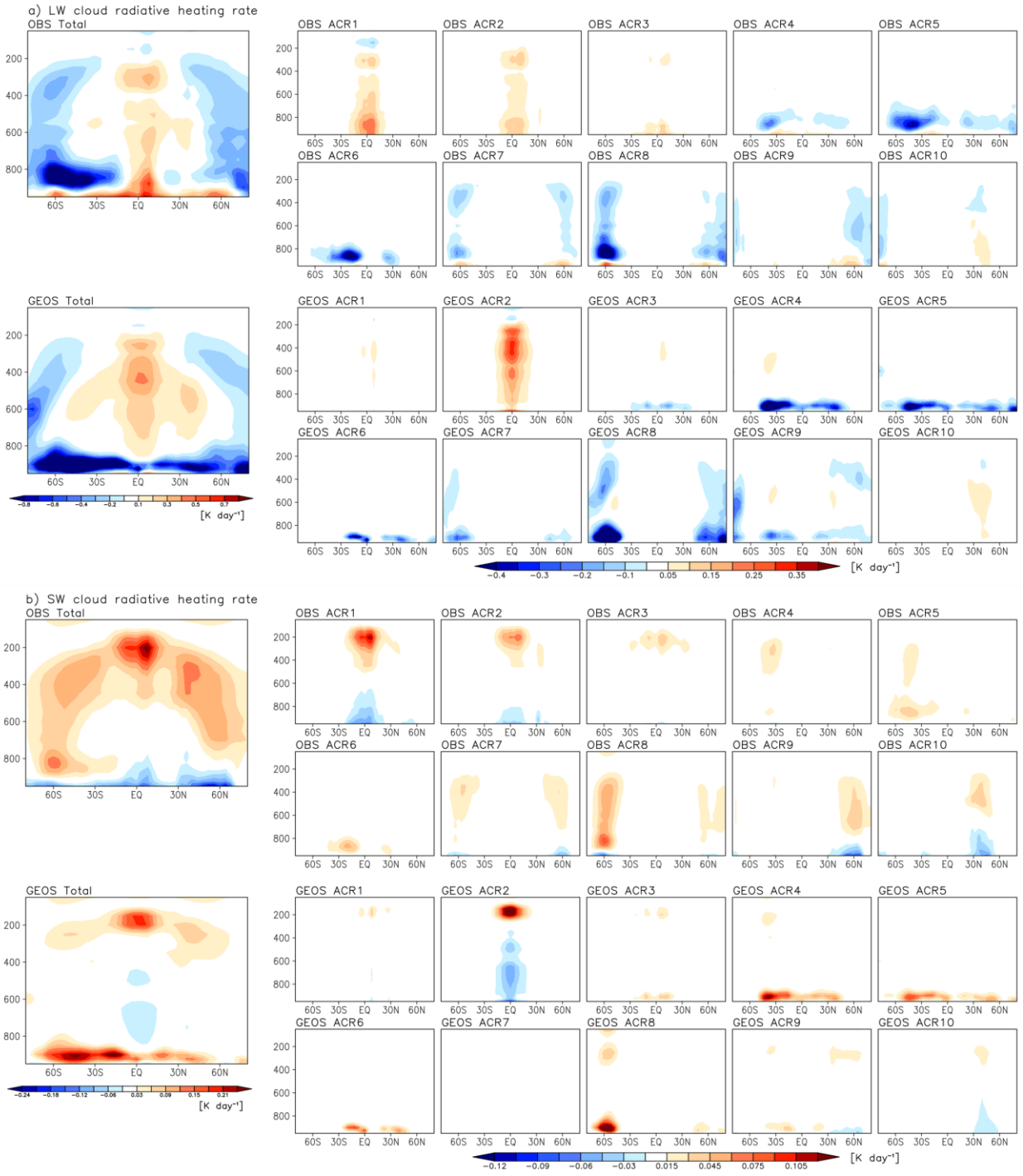


395

**Figure 7.** (a) Zonal-height plots of the annual LW CRHR corresponding to the 10 ACRs; (b) Same as (a), but for SW CRHR. For both the LW and SW CRHR, the top two rows of panels correspond to observations while the bottom two rows correspond to GEOS. In both figures the LW and SW zonal-height CRHR distribution regardless of ACR is also shown (the bigger panels on the left).

The top two rows of Fig. 7a reveal that ACR1-ACR3 have a radiative warming effect, i.e., induce a reduction in the rate of clear-sky radiative cooling, on a range of tropospheric altitudes. Other than the highest tropospheric levels where there is enhanced (relative to cloudy skies) cloud emission to space and thus enhanced cooling, ACR1 suppresses the atmospheric cooling in the rest of the troposphere by enhanced downward emission counteracting upward emission, i.e., reducing the efficiency of radiative cooling. ACR2 exhibits weaker cooling reduction and no measurable upper tropospheric cooling since its highest clouds are not as optically thick as those of ACR1. ACR3's clouds are not as vertically developed, hence their trapping and downward re-emission of LW radiation is much weaker. The other ACRs with substantial cloud amounts (ACR4-ACR9) enhance atmospheric LW radiative cooling (Fig. 5) to various degrees, with the exact profiles of radiative cooling enhancement depending on the exact CVSs that are prevalent within the ACR. For example, ACR6's cooling is much more concentrated in the lower troposphere because the dominance of CVS = *L* is stronger than for ACR8 which has also a considerable proportion of middle and low clouds (consolidated CVS = *ML* and CVS = *HML*)

Fig. 7b, the counterpart of Fig. 7a for SW, illustrates in the top two rows the observed enhancement or reduction at various tropospheric levels of clear-sky SW radiative heating. In general, ACRs enhance SW radiative heating because of the additional solar absorption provided by cloud particles, except at low altitudes where reduction in heating can occur as overlying

clouds block radiation that would have otherwise propagated to the lower tropospheric levels where boundary layer clouds and low-level water vapor await to induce absorption. When there are no substantial amounts of overlying high clouds such in ACR6, the solar absorption added by clouds manifests only in the lower troposphere where most clouds reside.

The bottom two rows of panels of the two parts of Fig. 7 show the decomposition of CRHR by ACR in GEOS. We first note that the overall CRHR height-latitude distribution in GEOS differs substantially from observations. GEOS's LW CRHR plots reveal a pervasive absence of middle and high clouds to prevent or temper the LW cooling of the lowermost clouds. As a result, low cloud cooling is present at all latitudes and confined to the lowest 200 hPa of the troposphere. On the SW side, the absence of middle-level clouds and the overall smaller amounts of low clouds close to the top of the boundary layer or just above it, suppresses the cooling that would have occurred due to reduced water vapor absorption in the lowermost troposphere. Instead, SW absorption takes place by the boundary layer clouds themselves either when there is not much overlying cloudiness to dampen the downward propagation of solar flux (ACR4, ACR5, and ACR6), or even when there is (ACR8).

### *5.3 Atmospheric Diabatic Heating*

The breakdown by ACR of the atmospheric diabatic heating and its three components (latent heating LH, atmospheric radiative cooling $Q_r$, and sensible heating SH) according to observations/reanalysis and GEOS are shown in Fig. 8. Observed LH (green bars) comes from GPCP monthly precipitation (Version 3.2, Huffman et al., 2023) values converted to $Wm^{-2}$ by multiplying the rain rates with the latent heat of vaporization using an approximate relationship, instead of surface evaporative fluxes. The observed $Q_r$ (blue bars) is the atmospheric radiative flux divergence and is calculated from CERES EBAF Ed4.2 as the difference between TOA and

surface combined SW and LW all-sky net (=down-up) fluxes. SH (green bars) comes from MERRA-2 reanalysis (GMAO 2015, Gelaro et al., 2017). The values shown have been weighted by the annual global RFO of each ACR, so represent ACR contributions to global values of diabatic heating and its components (i.e., they yield the proper global value when added). The corresponding GEOS values are shown with open circle symbols.

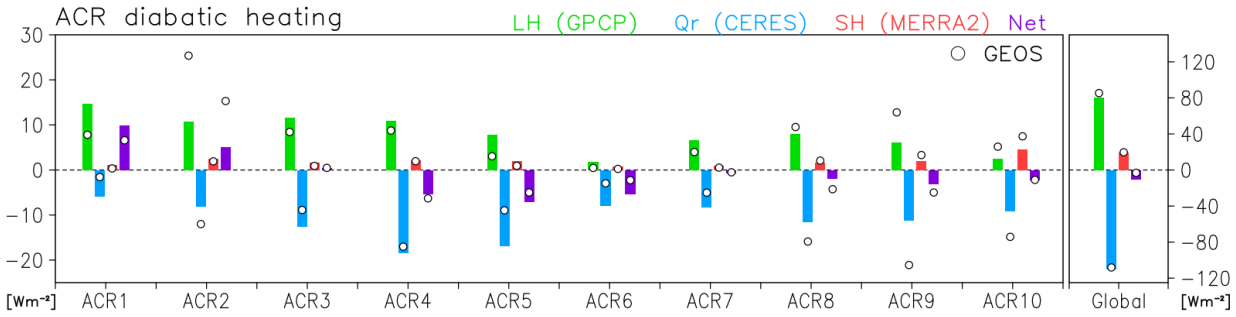


**Figure 8.** The observed total atmospheric diabatic heating (purple bars) and its components latent heat LH, radiative flux divergence $Q_r$, and sensible heat SH (green, blue, red bars, respectively). Counterpart values for the atmospheric GEOS model are shown as open circles. Global values irregardless of ACR are shown in the rightmost part of the plot.

According to Fig. 8, only the two mostly tropical ACRs, ACR1 and ACR2 have positive diabatic heating mainly because of the small $Q_r$ in the presence of plentiful high clouds that have a positive ATM CRE. ACR1's convection not only reduces greatly (in absolute terms) $Q_r$, but also produces large amounts of precipitation, and thus yields the largest diabatic heating. The largest (in absolute terms) contribution to the (negative) global $Q_r$ does not coincide with the ACR that has the largest proportion of CVS = *L* clouds (ACR6), but rather with ACR4 which is much more prevalent. ACR6 is though associated with the lowest precipitation, making its diabatic heating substantially negative, as there is not much counteraction for the negative $Q_r$. Despite

460 higher precipitation than ACR6, ACR5's negative total diabatic heating (the largest of all ACRs)
461 is larger because the radiative cooling added by its clouds is so much larger.

462 The global diabatic heating shown in the rightmost part of the plot is near-zero (within the
463 uncertainties of the datasets), as expected, in accordance with the planet being in radiative-
464 convective equilibrium, where the atmospheric radiative cooling is compensated by the surface
465 turbulent fluxes (or their atmospheric surrogates). The GEOS global values agree well with
466 observations despite large disagreements in the breakdown by ACR. Particularly striking is the
467 completely different energy distribution of GEOS for ACR1 and ACR2. The model's version of
468 ACR1 produces much less precipitation for ACR1, but compensates with excessive precipitation
469 for ACR2 despite the fact that its ratio of CVS = *HML* to CVS = *H* clouds is much lower than
470 observations, which in turns implies that modeled CVS = *H* clouds are strong precipitation
471 producers. Combined with a larger reduction of $Q_r$ in GEOS, the total diabatic heating of ACR2
472 in GEOS is more than twice as large as in observations and actually overcompensates for the
473 underestimate of diabatic heating by ACR1.

474 Figure 9 shows the contribution of each ACR to the annual zonal variation of two main adiabatic
475 heating components ($Q_r$ and LH) in the same manner as Fig. 6. The left column of panels
476 corresponds to observations while the right column to GEOS; the bottom row of panels shows
477 the zonal variation of ACR RFO. While the zonal distributions of the cumulative $Q_r$ and LH (i.e.,
478 regardless of ACR) are quite similar between observations and model, ACR contributions are
479 quite dissimilar. The diminished role in GEOS of ACR1 relative to that of ACR2 is again clearly
480 seen in the tropics for both $Q_r$ and LH. ACR8 and ACR9 are bigger contributors in the model's

481 Northern Hemisphere than in observations because of their larger RFOs; ACR5 is a much
482 smaller contributor everywhere compared to observations because of its global scarcity.

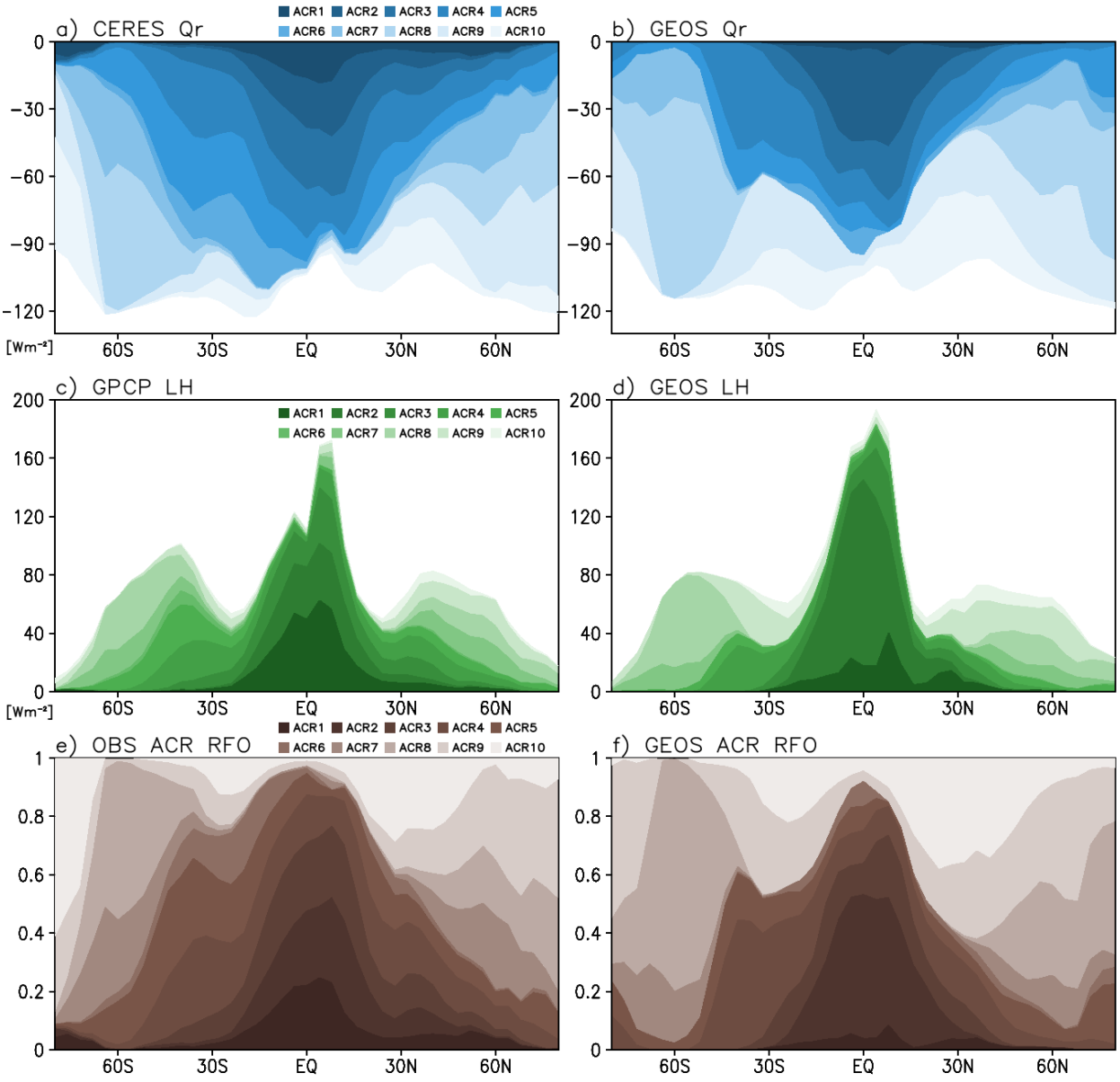


483

484 **Figure 9.** Contributions by ACR to the zonal variation of the two main adiabatic heating
485 components ($Q_r$ and LH) shown in the same manner as Fig. 6. The left column of panels
486 corresponds to observations while the right column to GEOS; the bottom row of panels shows
487 the zonal variation of ACR RFO.

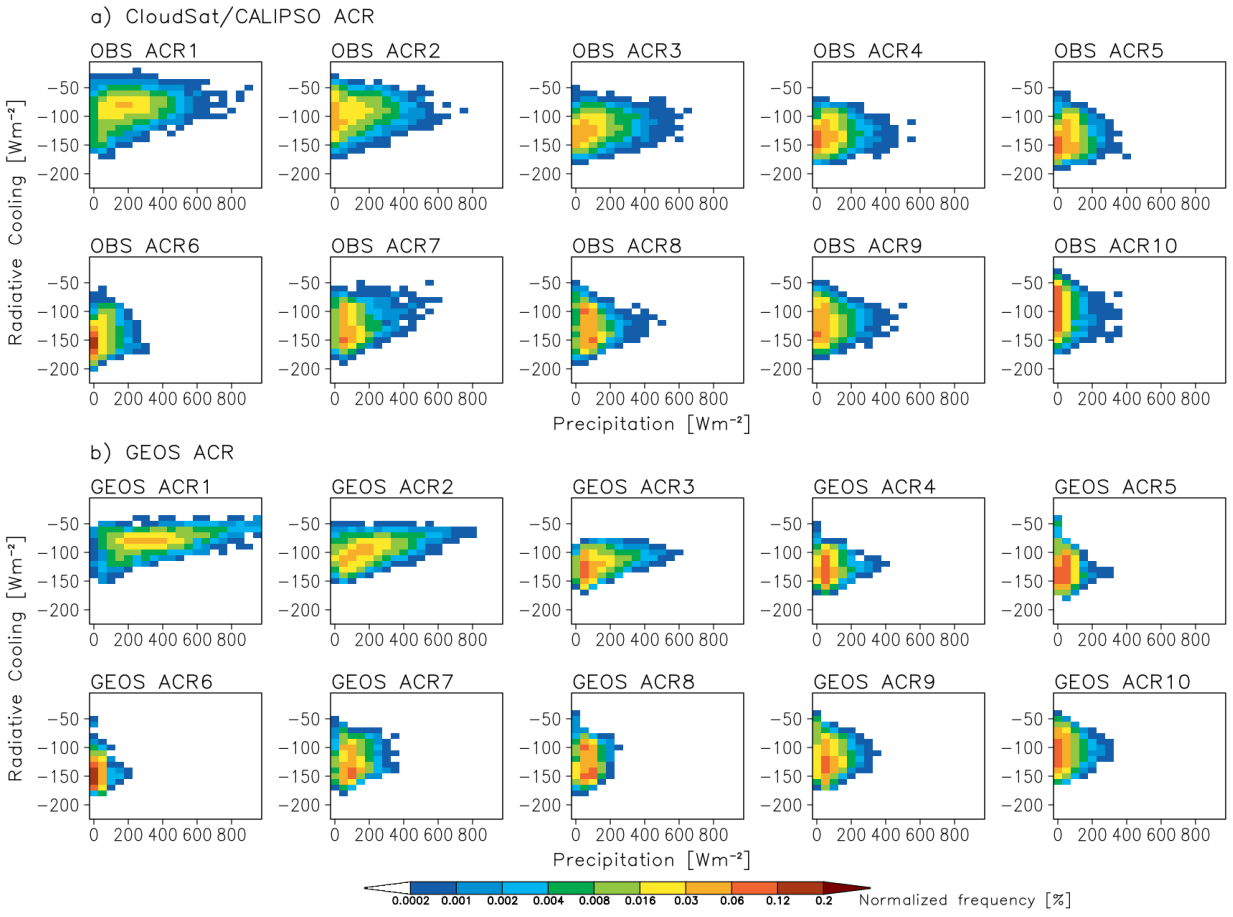


**Figure 10.** Density plots of the two major diabatic heating components, namely atmospheric flux divergence (radiative cooling) vs latent heat (i.e., precipitation in $Wm^{-2}$) for the 10 ACRs. The top two rows of panels (a) correspond to observations, while the bottom two rows (b) to GEOS.

Joint histograms (density plots) of $Q_r$ (from CERES-EBAF Ed4.2, as above) and precipitation (LH) from GPCP are shown in Fig. 10. This type of plot was introduced by Jakob et al. (2019) to elucidate how the competition between radiative cooling and latent heating due to precipitation results in a radiative-convective quasi-equilibrium state in the tropics. At first glance, it appears that the model's density plots exhibit substantial resemblance to observations, but more careful comparison reveals several differences. It is interesting that despite the overall weaker precipitation of its ACR1, the model produces occasionally extreme high values not seen in the

observations. One should however not place unwarranted attention to these extremes as they are quite rare (note the colorbar's logarithmic scale). The same also happens to some extent for ACR2. For the remaining ACRs the opposite is true, with the real world having a wider precipitation range. A wider range of values in observations is also seen for atmospheric cooling, although once again, this impression is exaggerated by the non-linear color scale. The model's overestimation of precipitation for ACR2 and ACR9 is seen here as a rightward shift of peak populations. On the flipside, these ACRs have smaller populations in the weak radiative cooling part of the phase space, reflecting the overestimation of radiative cooling needed to compensate for the exaggerated precipitation.

## 6. Discussion and conclusions

We propose a new way to characterize sub-seasonal (monthly) cloudiness over large ~400 km regions that essentially classifies recurrent patterns of cloud vertical morphology. The coarse spatial resolution is a necessary compromise that previous investigators (Haynes et al 2013; L'Ecuyer et al 2019; Hang et al 2019) had to also accept when presenting climatological cloud characteristics from spatially sparse CloudSat and CALIPSO observations. We show that 10 classes of so-called active cloud regimes (ACRs) describe effectively and meaningfully where and how frequently different types of vertical cloud configuration coexist in approximately recurrent proportions. We demonstrate that the ACRs are particularly suitable for understanding the radiative impacts of different cloud vertical structure mixtures, namely their relative contributions to planetary and surface cooling and to enhancements or reductions of the full-column and vertically resolved radiative cooling of the atmosphere. Furthermore, we used ACRs

as a foundational dataset to understand different states of the competition between atmospheric radiative cooling and latent heating.

Simulating realistic ACRs in Global Climate Model is a stringent requirement that cannot even be assessed unless the model can produce CVS, which in turn requires a cloud subcolumn generator. NASA's GEOS implements such a generator, but when it comes to producing credible CVS the model has mixed success (Lee et al. 2020). This is not only because of the generator's inadequacies, but also (primarily) of the flawed cloud fraction profiles supplied to the generator. When CVS are unrealistic, so will also inexorably be ACRs. Therefore, when assessed in terms of ACRs, GEOS does not seem to have enough vertically developed clouds, has too many isolated high clouds which produce unphysical amounts of precipitation, lacks mid-level clouds, and forms low clouds too close to the surface. Its global energetics are good, but the breakdown of energy fluxes by ACR deviates from the real world.

We view ACRs as complementary to cloud classifications based on passive observations such as cloud regimes (CRs; Oreopoulos et al. 2014; Oreopoulos et al. 2016; Cho et al. 2021) and regimes of regimes (RORs; Cho et al 2024, accepted manuscript). While ACRs contain information about the vertical structure of clouds, they do not explicitly contain information on cloud opacity which primarily controls propagation of solar radiation. While cloud vertical extent correlates with opacity, there is no strict one-to-one correspondence since hydrometeor concentrations can vary widely. Passively-derived CRs are similarly deficient in providing unambiguous descriptions of how clouds interact with thermal infrared radiation, especially when it comes to radiation emitted towards the surface. Thus both active and passive classifications have to be used synergistically for a more complete picture of cloud climatologies, and to understand better how broad cloud classes regulate the planet's energy budget. We plan to

543 conduct such work in the future, conceivably under a framework of hybrid passive-active cloud
544 regimes.

545 **Acknowledgments**

546 Resources supporting this work were provided by the NASA High-End Computing (HEC)
547 Program through the NASA Center for Climate Simulation (NCCS) at Goddard Space Flight
548 Center. Support by NASA's CloudSat-CALIPSO Science Team program is gratefully
549 acknowledged.

550

551 **Open Research**

552 Observed CVS, and observed/modeled ACRs and the data used to produce the manuscript's
553 figures are available at https://doi.org/10.5281/zenodo.13891853. The 2B-CLDCLASS-LIDAR
554 and 2B_FLXHR-LIDAR datasets are available at http://www.cloudsat.cira.colostate.edu/ and
555 CERES EBAF Ed4.2 dataset (NASA/LARC/SD/ASDC., 2023) is available at
556 https://ceres.larc.nasa.gov/data/. GPCP v3.2 dataset (Huffman et al., 2022) can be downloaded
557 from https://measures.gesdisc.eosdis.nasa.gov/data/GPCP/GPCPMON.3.2/. MERRA-2
558 tavgM_2d_flx_Nx dataset (GMAO, 2015) is available at
559 https://goldsmr4.gesdisc.eosdis.nasa.gov/data/MERRA2_MONTHLY/M2TMNXFLX.5.12.4/.
560 The baseline GEOS model source code can be accessed at https://github.com/GEOS-
561 ESM/GEOSgcm/releases/tag/v10.21.0.

562

563 **References**

564 Cho, N., Tan, J., & Oreopoulos, L. (2021). Classifying planetary cloudiness with an updated set
565 of MODIS cloud regimes. *Journal of Applied Meteorology and Climatology, 60*(7), 981-997.

566 Gelaro, R., McCarty, W., Suárez, M. J., Todling, R., Molod, A., Takacs, L., Randles, C. A.,
567 Darmenov, A., Bosilovich, M. G., Reichle, R., Wargan, K., Coy, L., Cullather, R., Draper, C.,
568 Akella, S., Buchard, V., Conaty, A., da Silva, A. M., Gu, W., Kim, G., Koster, R., Lucchesi, R.,
569 Merkova, D., Nielsen, J. E., Partyka, G., Pawson, S., Putman, W., Rienecker, M., Schubert, S.
570 D., Sienkiewicz, M., & Zhao, B. (2017). The Modern-Era Retrospective Analysis for Research
571 and Applications, Version 2 (MERRA-2). *Journal of Climate*, *30*(14), 5419-5454.
572 https://doi.org/10.1175/JCLI-D-16-0758.1
573 Global Modeling and Assimilation Office (GMAO) (2015), MERRA-2 tavgM_2d_flx_Nx:
574 2d,Monthly mean,Time-Averaged,Single-Level,Assimilation,Surface Flux Diagnostics V5.12.4,
575 Greenbelt, MD, USA, Goddard Earth Sciences Data and Information Services Center (GES
576 DISC), Accessed: [05/30/2024], 10.5067/0JRLVL8YV2Y4
577 Hang, Y., L'Ecuyer, T. S., Henderson, D. S., Matus, A. V., & Wang, Z. (2019). Reassessing the
578 effect of cloud type on Earth's energy balance in the age of active spaceborne observations. Part
579 II: Atmospheric heating. *Journal of Climate*, *32*(19), 6219-6236.
580 Haynes, J. M., Vonder Haar, T. H., L'Ecuyer, T., & Henderson, D. (2013). Radiative heating
581 characteristics of Earth's cloudy atmosphere from vertically resolved active sensors. *Geophysical*
582 *Research Letters*, *40*(3), 624-630.
583 Henderson, D. S., L'Ecuyer, T., Stephens, G., Partain, P., & Sekiguchi, M. (2013). A multisensor
584 perspective on the radiative impacts of clouds and aerosols. *Journal of Applied Meteorology and*
585 *Climatology*, *52*(4), 853-871.
586 Huffman, G. J., Adler, R. F., Behrangi, A., Bolvin, D. T., Nelkin, E. J., Gu, G., & Ehsani, M. R.
587 (2023). The New Version 3.2 Global Precipitation Climatology Project (GPCP) Monthly and
588 Daily Precipitation Products. *Journal of Climate*, *36*(21), 7635-7655.
589 https://doi.org/10.1175/JCLI-D-23-0123.1

590 Huffman, G.J., A. Behrangi, D.T. Bolvin, E.J. Nelkin (2022), GPCP Version 3.2 Satellite-Gauge
591 (SG) Combined Precipitation Data Set, Edited by Huffman, G.J., A. Behrangi, D.T. Bolvin, E.J.
592 Nelkin, Greenbelt, Maryland, USA, Goddard Earth Sciences Data and Information Services
593 Center (GES DISC), Accessed: [05/30/2024], 10.5067/MEASURES/GPCP/DATA304
594 Jakob, C., Singh, M. S., & Jungandreas, L. (2019). Radiative convective equilibrium and
595 organized convection: An observational perspective. *Journal of Geophysical Research:*
596 *Atmospheres*, 124(10), 5418-5430.
597 Kato, S., F. G. Rose, D. A. Rutan, T. E. Thorsen, N. G. Loeb, D. R. Doelling, X. Huang, W. L.
598 Smith, W. Su, & Ham, S.-H. (2018) Surface irradiances of Edition 4.0 Clouds and the Earth's
599 Radiant Energy System (CERES) Energy Balanced and Filled (EBAF) data product. *Journal of*
600 *Climate, 31,* 4501–4527, doi:10.1175/JCLI-D-17-0523.1.
601 L'Ecuyer, T. S., Hang, Y., Matus, A. V., & Wang, Z. (2019). Reassessing the effect of cloud type
602 on Earth's energy balance in the age of active spaceborne observations. Part I: Top of atmosphere
603 and surface. *Journal of Climate, 32*(19), 6197-6217.
604 Lee, D., Oreopoulos, L., & Cho, N. (2020). An evaluation of clouds and radiation in a large-scale
605 atmospheric model using a cloud vertical structure classification. *Geoscientific Model*
606 *Development, 13*(2), 673-684.
607 Loeb, N. G., D. R. Doelling, H. Wang, W. Su, C. Nguyen, J. G. Corbett, L. Liang, C. Mitrescu,
608 F. G. Rose, & Kato, S. (2018). Clouds and the Earth's Radiant Energy System (CERES) Energy
609 Balanced and Filled (EBAF) top-of-atmosphere (TOA) edition-4.0 data product. *Journal of*
610 *Climate, 31*(2), 895–918.
611 Matus, A. V., & L'Ecuyer, T. S. (2017). The role of cloud phase in Earth's radiation budget.
612 *Journal of Geophysical Research: Atmospheres, 122*(5), 2559-2578.

NASA/LARC/SD/ASDC. (2023). CERES Energy Balanced and Filled (EBAF) TOA and Surface Monthly means data in netCDF Edition 4.2 [Data set]. NASA Langley Atmospheric Science Data Center DAAC. Retrieved from https://doi.org/10.5067/TERRA-AQUA-NOAA20/CERES/EBAF_L3B004.2

Oreopoulos, L., Cho, N., Lee, D., Kato, S., & Huffman, G. J. (2014). An examination of the nature of global MODIS cloud regimes. *Journal of Geophysical Research: Atmospheres, 119*(13), 8362-8383.

Oreopoulos, L., Cho, N., Lee, D., & Kato, S. (2016). Radiative effects of global MODIS cloud regimes. *Journal of Geophysical Research: Atmospheres, 121*(5), 2299-2317.

Oreopoulos, L., Cho, N., & Lee, D. (2017). New insights about cloud vertical structure from CloudSat and CALIPSO observations. *Journal of Geophysical Research: Atmospheres, 122*(17), 9280-9300.

Räisänen, P., Barker, H. W., Khairoutdinov, M. F., Li, J., & Randall, D. A. (2004). Stochastic generation of subgrid-scale cloudy columns for large-scale models. *Quarterly Journal of the Royal Meteorological Society, 130*(601), 2047-2067.

Rienecker, M. M., Suarez, M. J., Todling, R., Bacmeister, J., Takacs, L., Liu, H.-C., et al. (2008). The GEOS-5 data assimilation system—Documentation of versions 5.0.1, 5.1.0, and 5.2.0. *NASA Technical Reports* Series on Global Modeling and Data Assimilation, NASA/TM-2008-104606, Vol.27, 92 pp, *NASA Technical reports*.

Rossow, W. B., & Schiffer, R. A. (1999). Advances in understanding clouds from ISCCP. *Bulletin of the American Meteorological Society, 80*(11), 2261-2288.

Sassen, K., Wang, Z. & Liu, D.(2008). Global distribution of cirrus clouds from CloudSat/Cloud-Aerosol lidar and infrared pathfinder satellite observations (CALIPSO) measurements. *Journal of Geophysical Research: Atmospheres, 113*(D8).

637 Stephens, G.L., Vane, D.G., Boain, R.J., Mace, G.G., Sassen, K., Wang, Z., Illingworth, A.J.,
638 O'connor, E.J., Rossow, W.B., Durden, S.L. & Miller, S.D. (2002). The CloudSat mission and
639 the A-Train: A new dimension of space-based observations of clouds and precipitation. *Bulletin*
640 *of the American Meteorological Society*, *83*(12), pp.1771-1790.
641 Winker, D.M., Vaughan, M.A., Omar, A., Hu, Y., Powell, K.A., Liu, Z., Hunt, W.H. & Young,
642 S.A.(2009). Overview of the CALIPSO mission and CALIOP data processing
643 algorithms. *Journal of Atmospheric and Oceanic Technology*, *26*(11), pp.2310-2323.